Imaging vertical structures using Marchenko methods with vertical seismic-profile data

Imaging Vertical Structures using Marchenko Methods with Vertical Seismic Profile Data

Angus Lomas*, **Satyan Singh*** **and Andrew Curtis***

**School of GeoSciences, University of Edinburgh,*

Grant Institute, James Hutton Road,

King's Buildings, Edinburgh, UK, EH9 3FE

(March 22, 2020)

Running head: **Marchenko Methods with VSP Data**

ABSTRACT

Marchenko methods use seismic data acquired at or near the surface of the Earth to estimate seismic signals as if the receiver (now a *virtual* receiver) was at an arbitrary point inside the subsurface of the Earth. This process is called redatuming and is central to subsurface imaging. Marchenko methods estimate the multiply scattered components of these redatumed signals, which is not the case for most other redatuming techniques which are based on single-scattering assumptions. As a result, images created using Marchenko redatumed signals contain a reduction in the artifacts that usually contaminate migrated seismic images due to improper handling of internal multiples. We exploit recent theoretical advances that enable both virtual sources and virtual receivers to be placed at arbitrary points inside the subsurface as a means to incorporate vertical seismic profile (VSP) data into Marchenko methods. The advantage of including this type of data is that the additional acquisition boundary increases subsurface illumination, which in turn enables vertical interfaces and steeply dipping structures to be imaged. We demonstrate this methodology on two synthetic datasets. The first dataset is created using a simple variable density but constant velocity subsurface model. We show in this example that our newly devised VSP Marchenko imaging methodology enables imaging of both horizontal and vertical structures and that optimal results are achieved by combining these images with those created using standard Marchenko imaging. A second example demonstrates that the method can be applied to more realistic subsurface structures, in this case a modified version of the *Marmousi 2* model. We show the applicability of the methods to image fault structures with the final imaging result containing reduced contamination due to internal multiples and an improvement in the imaging of fault structures when compared to other standard imaging methods alone.

INTRODUCTION

Marchenko methods are used in geophysics to redatum receivers that are physically located on the Earth's surface to arbitrary virtual receiver positions inside the subsurface. The methods estimate the seismograms that would have been recorded at those new positions if physical receivers had been placed there. Marchenko methods have applications that include target oriented imaging (Behura et al., 2014; Wapenaar et al., 2014; Ravasi et al., 2016), redatuming (Wapenaar et al., 2014; Ravasi, 2017) and internal multiple attenuation (Meles et al., 2014, 2016; da Costa Filho et al., 2017). Their advantage over most other redatuming methods is that they account for the reverberations of waves within the Earth (so-called internal multiples) using just single-sided illumination of the subsurface and a smooth estimate of the subsurface velocity structure. The original implementations of these techniques, which we follow in this article, focus on acoustic problems with an absorbing surface boundary (Broggini et al., 2012; Wapenaar et al., 2013). However, more recent applications have extended the methodology to elastic media (da Costa Filho et al., 2014, 2015) and data containing free surface multiples (Singh et al., 2015, 2016; Ravasi, 2017; Slob and Wapenaar, 2017). The aim of the work in this article is to incorporate the additional information available from vertical seismic profile (VSP) data to improve Marchenko estimates of Green's functions, thereby improving the final images of the Earth's subsurface.

A recent theoretical advance in this field is so-called 'Marchenko source-receiver redatuming'. These methods use receiver-redatumed Green's functions calculated using Marchenko methods to also redatum the source to a second arbitrary subsurface location (Wapenaar et al., 2016; Singh and Snieder, 2017; Wapenaar et al., 2018). In this article we propose that the receiver redatumed signals can be replaced with a measured VSP signal. The advantage

of including this type of data is that it enables more accurate Green's functions to be calculated. In particular, wavefield components can be constructed to which the Marchenko method alone is insensitive – in this case reflections from vertical or near vertical interfaces. This in turn will allow Marchenko images to be produced that identify vertical and steeply-dipping subsurface features while retaining the ability to image sub-horizontal structures and reduce internal multiple contamination.

Previous studies incorporating seismic data measured by downhole receivers into Marchenko methods aimed to reduce the sensitivity of Marchenko methods to velocity model errors (Liu et al., 2016), to estimate the scaling factor of reflection data, which is normally a prerequisite for applying Marchenko methods (Van Der Neut et al., 2015; Thomsen et al., 2017), or to develop novel methods for wavefield separation (Liu et al., 2018). In all of these examples the downhole receivers are used as an additional control when calculating standard Marchenko Green's functions. None of these methods exploit the additional full wavefield recordings available from the downhole receivers.

The virtual source method proposed by Bakulin and Calvert (2006) demonstrated the applicability of interferometric concepts to use data measured downhole to redatum sources to create virtual sources inside the well. This method is advantageous as it is able to account for complexities in the overburden without requiring an accurate estimate of the velocity model. A similar approach was taken by Hornby and Yu (2007) to image the flank of salt structures. Comparisons between methods like these and source-receiver Marchenko redatuming methods have previously been analysed by Singh and Snieder (2017).

Alternative methods for imaging vertical interfaces have also been proposed: Xu and Jin (2006) suggested using wave equation migration of diving waves to image the flank of

salt structures and Malcolm et al. (2009) showed that vertical interfaces can be mapped using multiply scattered seismic waves, surface seismic data and wave equation migration when abrupt interfaces are correctly included in the input velocity model. For both of these methods an exceptionally accurate velocity model is required for accurate reflector mapping, and internal multiple contamination in the final images remains a problem. More recently Zuberi and Alkhalifah (2014) suggested using multiply-scattered waves measured in surface seismic data (duplex waves) to image vertical and near vertical interfaces, but the results were shown to be prone to contamination by artifacts. Finally, Singh and Curtis (2019) also used surface seismic data and so-called time-reverse mirror imaging (TRMI) which uses an autocorrelation imaging condition: this methodology was shown to accurately image vertical interfaces but was insensitive to horizontal features.

In this article we first introduce the standard Marchenko theory, how this relates to the more recent 'virtual source-virtual receiver' developments, and our approach to incorporate VSP data. We then analyse the impacts of a vertical interface on standard Marchenko estimates, which are shown to produce poor reconstructions of wavefield components created by vertically orientated subsurface features. We then focus on the VSP application: we use the new method to construct improved subsurface seismic wavefield estimates, then use this wavefield for seismic imaging. The images created as a result are accurate and would be unobtainable with existing alternative imaging methods alone.

MARCHENKO METHODS

Marchenko Receiver Redatuming

Standard Marchenko methods require seismic reflection data measured at co-located source and receiver positions on or near the surface of the Earth (R), and an estimated model of the subsurface velocity structure. The methods calculate directionally decomposed seismograms (the pressure recording in response to a volume injection rate source) – which are referred to herein as (band-limited) Green's functions ($G^{+/-}(\mathbf{x}_i, \mathbf{x}_0, \omega)$) – between the surface source positions ($\mathbf{x}_0$) and an arbitrarily chosen virtual receiver position ($\mathbf{x}_i$) inside the subsurface. Throughout this article these are expressed in the frequency domain (ω). Directional decomposition is in the observed direction of wave propagation as it is measured at the receiver, and in all cases + denotes downgoing and − denotes upgoing waves. The equations that govern the relationship between the reflectivity (R) and the Green's functions of interest are:

$$G^{-}(\mathbf{x}_i, \mathbf{x}_0, \omega) = \int_{\partial \mathbb{D}_0} R(\mathbf{x}_0, \mathbf{x}_0', \omega) f_1^{+}(\mathbf{x}_0', \mathbf{x}_i, \omega) d\mathbf{x}_0' - f_1^{-}(\mathbf{x}_0, \mathbf{x}_i, \omega), \tag{1}$$

$$G^{+}(\mathbf{x}_i, \mathbf{x}_0, \omega) = f_1^{+}(\mathbf{x}_0, \mathbf{x}_i, \omega)^{*} - \int_{\partial \mathbb{D}_0} R(\mathbf{x}_0, \mathbf{x}_0', \omega) f_1^{-}(\mathbf{x}_0', \mathbf{x}_i, \omega)^{*} d\mathbf{x}_0'. \tag{2}$$

Each of the terms in equations 1 and 2 is a function of two sets of spatial locations: $\mathbf{x}_0$ represents an array of points on the boundary $\partial \mathbb{D}_0$ with a fixed depth coordinate $z = 0$ m and a variable horizontal coordinate, $\mathbf{x}_0 = \{(x_j, y_j, 0) : j = 1, 2, \ldots, N\}$ where N is the number of source/receiver positions, and for this formulation the set of points in $\mathbf{x}_0$ have to be the same as those in $\mathbf{x}_0'$. Location $\mathbf{x}_i = (x, y, i)$ represents a point on the constant depth

boundary $\partial\mathbb{D}_i$. Here f_1 denotes a so-called focusing function: the downgoing component of this function is defined such that when it is injected as a source time function into the true subsurface model it will collapse at zero time to an impulse at the virtual source location (Slob et al., 2014). The upgoing component of the focusing function is the measured response at the surface to the injection of the downgoing functions. However, this is only the case in a truncated medium which is defined to be equal to the true medium above the boundary $\partial\mathbb{D}_i$, and is homogeneous below this depth. We calculate these functions using the iterative solution to the coupled Marchenko equations (Wapenaar et al., 2014) and we refer readers to Lomas and Curtis (2019) for an intuitive introduction and more details on this method.

The theoretical foundation of equations 1 and 2 are the one-way reciprocity theorems of the convolution and correlation type for pressure normalized one-way wavefields (Wapenaar and Grimbergen, 1996; Wapenaar et al., 2014):

$$-\int_{\partial\mathbb{D}_0}\frac{1}{\rho(\mathbf{x}_0')}\ \left[p_A^+(\partial_z p_B^-)+p_A^-(\partial_z p_B^+)\right]\ d\mathbf{x}_0'=\int_{\partial\mathbb{D}_i}\frac{1}{\rho(\mathbf{x}_i')}\ \left[(\partial_z p_A^+)p_B^-+(\partial_z p_A^-)p_B^+\right]\ d\mathbf{x}_i', \quad (3)$$

$$-\int_{\partial\mathbb{D}_0}\frac{1}{\rho(\mathbf{x}_0')}\ \left[p_A^{+*}(\partial_z p_B^+)+p_A^{-*}(\partial_z p_B^-)\right]\ d\mathbf{x}_0'=\int_{\partial\mathbb{D}_i}\frac{1}{\rho(\mathbf{x}_i')}\ \left[(\partial_z p_A^+)^* p_B^+ +(\partial_z p_A^-)^* p_B^-)\right]\ d\mathbf{x}_i'. \quad (4)$$

Equations 3 and 4 are given in the frequency domain, subscripts A and B refer to two different acoustic states, $p_{A/B}$ represents a wavefield in the state defined by their subscript, ∂_z represents the vertical derivative of the corresponding wavefield and superscript $*$ denotes complex conjugation (or time reversal). Furthermore, these equations only hold under

certain conditions: first there can not be any energy source at a depth level between the boundary $\partial\mathbb{D}_0$ and the boundary $\partial\mathbb{D}_i$, evanescent waves are not present in any of the measured wavefields, and for equation 4 to hold the medium needs to be lossless between the boundary $\partial\mathbb{D}_0$ and the boundary $\partial\mathbb{D}_i$.

If we take state A to be the state in which the focusing functions exist in the truncated medium and state B to be the Green's functions state in the true medium we can assign the values $p_A^{+/-} = f_1^{+/-}(\mathbf{x}_0'/\mathbf{x}_i', \mathbf{x}_i, \omega)$ and $p_B^{+/-} = G^{+/-}(\mathbf{x}_0'/\mathbf{x}_i', \mathbf{x}_0, \omega)$ where the receiver position is defined by the corresponding boundary integral, in this context the symbol / means 'or'. Following the method in Appendix A of Wapenaar et al. (2014) these wavefields can be substituted into equations 3 and 4 to form equations 1 and 2.

Marchenko Source-Receiver Redatuming

The previous section describes equations 1 and 2 which are used as part of the Marchenko method to construct signals between the surface acquisition array and subsurface virtual receivers. More recent work has shown how we can use the estimated Marchenko Green's functions to redatum the Green's functions as if the source was also at an arbitrary point inside the subsurface, so-called Marchenko source-receiver redatuming. This work is the natural extension of source-receiver interferometric methods of Curtis and Halliday (2010) and Halliday and Curtis (2010) to the case of single-sided acquisition and Marchenko methods. It was pioneered by Wapenaar et al. (2016) and Singh and Snieder (2017) and has recently been applied to real field data (Wapenaar et al., 2018), and extended to elastodynamic applications (Urruticoechea and Wapenaar, 2017).

In this article we suggest a method to incorporate VSP data into the source-receiver

method. The advantage of doing this is that we overcome a limitation of the Marchenko method – the ability to handle steeply dipping subsurface interfaces, which ultimately allows us to obtain more accurate Green's functions. In particular this enables the Marchenko method to better construct virtual-source virtual-receiver Green's functions, and thus to produce improved seismic images of vertical or near-vertical interfaces.

Here we follow the implemetation of the technique of Singh and Snieder (2017), however we have simplified the problem by assuming that there are no free-surface multiples present in the data (i.e. that surface-related multiples have been removed from recorded data). However, this is not a limitation of the method we introduce in this article and the methodology can be applied to the case where the seismic data does contain free-surface multiples.

The relationship between the measured Green's functions from the previous section and the Green's functions of interest here are retrieved by substituting the wavefields from Table 1 into the modified reciprocity theorems from equations 3 and 4 ($d\mathbf{x}_0' \rightarrow d\mathbf{x}_0$). If ι is the imaginary unit, ω is angular frequency and ρ is density then:

[Table 1 about here.]

$$G^{-}(\mathbf{x}_i, \mathbf{x}_j, \omega) = \int_{\partial \mathbb{D}_0} \frac{2}{\iota \omega \rho(\mathbf{x}_0)} \partial_z G(\mathbf{x}_0, \mathbf{x}_j, \omega) f_1^{+}(\mathbf{x}_0, \mathbf{x}_i, \omega) d\mathbf{x}_0, \tag{5}$$

$$G^{+}(\mathbf{x}_i, \mathbf{x}_j, \omega) = -\int_{\partial \mathbb{D}_0} \frac{2}{\iota \omega \rho(\mathbf{x}_0)} \partial_z G(\mathbf{x}_0, \mathbf{x}_j, \omega) f_1^{-}(\mathbf{x}_0, \mathbf{x}_i, \omega)^{*} d\mathbf{x}_0. \tag{6}$$

If we sum equations 5 and 6 we obtain:

$$G(\mathbf{x}_i, \mathbf{x}_j, \omega) = \int_{\partial \mathbb{D}_0} \frac{2}{\iota \omega \rho(\mathbf{x}_0)} \partial_z G(\mathbf{x}_0, \mathbf{x}_j, \omega) f_2(\mathbf{x}_i, \mathbf{x}_0, \omega) d\mathbf{x}_0, \tag{7}$$

where $f_2(\mathbf{x}_i, \mathbf{x}_0, \omega) = f_1^+(\mathbf{x}_0, \mathbf{x}_i, \omega) - f_1^-(\mathbf{x}_0, \mathbf{x}_i, \omega)^*$. Equations 5-7 only hold if point $\mathbf{x}_i$ is at a depth above $\mathbf{x}_j$: $i < j$. In other words the virtual source term in the Green's functions needs to be below the virtual receiver term of the focusing functions. When both the Green's functions and the focusing functions are estimated using Marchenko methods these are interchangeable (by source-receiver reciprocity) and analogous equations exist when the depth coordinates satisfy $i > j$. However, in our implementation we propose that the Marchenko estimate of $G(\mathbf{x}_0, \mathbf{x}_j, \omega)$ be replaced by the approximation to the Green's function measured in a VSP survey. In doing so the location $\mathbf{x}_j$ and the G term cannot be changed: so when we implement equation 7 we can only construct Green's functions between arbitrarily chosen virtual receiver positions and the fixed VSP receivers (now virtual sources) inside the well.

We simplify equation 7 further given the definition of a particle velocity reponse to an impulsive point source of volume injection rate given by Wapenaar and Fokkema (2006):

$$v_z(\mathbf{x}_0, \mathbf{x}_j, \omega) = -\frac{1}{\iota \omega \rho(\mathbf{x}_0)} \partial_z G(\mathbf{x}_0, \mathbf{x}_j, \omega). \tag{8}$$

Here the volume injection rate sources are in the borehole and the particle velocity receivers are at the surface. However, by source-receiver reciprocity this is equivalent to a vertical force source at the surface and a pressure measurement in the borehole (Thorbecke et al., 2017). Substituting equation 8 into equation 7 then leads to:

$$G(\mathbf{x}_i, \mathbf{x}_j, \omega) = -2 \int_{\partial \mathbb{D}_0} v_z(\mathbf{x}_0, \mathbf{x}_j, \omega) f_2(\mathbf{x}_i, \mathbf{x}_0, \omega) d\mathbf{x}_0. \tag{9}$$

The original implementation of these methods proposed that both terms inside the integral in equation 9 can be estimated using Marchenko methods. The focusing function is calculated using the iterative Marchenko method (Wapenaar et al., 2014) and the Green's function is calculated by summing the results from equations 1 and 2. When using only inputs from previous Marchenko methods, the vertical particle velocity from equations 9 is not available and must be approximated (Wapenaar et al., 2017) – we discuss this in more detail below.

A limitation of using Marchenko Green's functions from equations 1 and 2 is that they are only able to accurately reconstruct the reflected components of the Marchenko Green's functions from equation 7 when the primary reflections from the structural features that caused them are measured at the surface of the Earth. Therefore, depending on the aperture of the seismic acquisition, equation 7 is often only accurate for near-horizontal subsurface structures. The object of our investigation is to obtain a subsurface image in cases where this assumption does not hold, as shown in Figure 1. Replacing the approximate Marchenko Green's function with the VSP Green's function therefore includes the potential to image more complex subsurface structures, whilst retaining the benefits of the Marchenko method to redatum wavefields and to account for the effects of internal multiples.

GREEN'S FUNCTION ESTIMATION

We first use a simple synthetic subsurface model to test these methods (Figure 1). This model has variable density but a constant velocity (2500 m/s) with several horizontal layers.

However, we have introduced a challenge for standard Marchenko imaging by including a vertical interface at $x = 1000$ m. Along the surface there are co-located sources and receivers at 16 m intervals which make up the acquisition array described by the vector of locations $\mathbf{x}_0$. Additionally, inside the subsurface, there is a VSP with receivers at variable depth positions, again spaced at 16 m intervals with a constant x coordinate of 1500 m.

[Figure 1 about here.]

Receiver Redatuming

As a first test we investigate the accuracy of Marchenko Green's function estimates for redatumed receivers with a vertical interface present in the subsurface (Figure 1). We first estimate the focusing functions, then use equations 1 and 2 to estimate Green's functions, and finally sum the result: $G(\mathbf{x}_i, \mathbf{x}_0, t) = G^+(\mathbf{x}_i, \mathbf{x}_0, t) + G^-(\mathbf{x}_i, \mathbf{x}_0, t)$. This is applied for a single surface source at (2004 m, 0 m) on the boundary $\partial\mathbb{D}_0$ and an array of receivers in the subsurface, the same receivers that make up the VSP (see Figure 1). The results are given in Figure 2 where we compare the estimated Marchenko Green's functions and the measured (directly modelled) Green's functions from the VSP.

[Figure 2 about here.]

Figure 2 shows that the Marchenko result gives accurate Green's functions for reflections from the horizontal subsurface layers. The accuracy of these signals is most apparent in Figure 2c where the match with the true solution is nearly perfect. This level of accuracy has also been demonstrated for other examples in previous literature (e.g. Wapenaar et al., 2013). However, components of the seismic wavefield that have interacted with the

vertical interface, marked by the red arrow, are not reconstructed and are missing from the Marchenko estimate of the VSP data. This result is to be expected because most of the energy that reflects from vertical interfaces follows paths down into the deeper Earth, hence is not recorded in surface seismic data and therefore can not be reconstructed by purely one-sided (ground-surface data driven) Marchenko methods (or any method that relies on primary reflections measured at the surface). The same focusing function term is used in equation 7 to produce both Figures 2a and 2b. This confirms that the focusing function is accurate (as it facilitates the accurate Green's function estimation in Figure 2b) and that the observed differences are due to the Green's functions on the right hand side of equation 7.

Source-Receiver Redatuming

We can use the results from Figure 2 to implement source-receiver redatuming using equation 7. The input to this equation is a vertical particle velocity measurement at the boundary $\partial\mathbb{D}_0$ in response to a volume injection rate source at point $\mathbf{x}_j$ in the subsurface (see equation 8 and 9). We can approximate the required response from the calculated Green's function in equations 1 and 2 and Figure 2a by making the approximation (Wapenaar and Fokkema, 2006):

$$\partial_z G(\mathbf{x}_0, \mathbf{x}_j, \omega) \approx -\frac{\iota\omega}{c(\mathbf{x}_0)} G(\mathbf{x}_0, \mathbf{x}_j, \omega). \tag{10}$$

We then substitute equation 10 into equation 7 to obtain:

$$G(\mathbf{x}_i, \mathbf{x}_j, \omega) \approx -\int_{\partial\mathbb{D}_0} \frac{2}{c(\mathbf{x}_0)\rho(\mathbf{x}_0)} G(\mathbf{x}_0, \mathbf{x}_j, \omega) f_2(\mathbf{x}_i, \mathbf{x}_0, \omega) d\mathbf{x}_0, \tag{11}$$

where c is velocity. These steps are similar to those taken to derive source-receiver interferometry (Curtis et al., 2009; Curtis and Halliday, 2010) which also provides alternative derivations of Green's functions between virtual sources and virtual receivers.

We can therefore implement equations 11 and 9 using the Marchenko-estimated and VSP-measured Green's functions to produce Figure 3a and 3b respectively. To do this we have arbitrarily chosen a subsurface source location at $\mathbf{x}_i = (1200\text{ m}, 600\text{ m})$ and calculated the focusing term $f_2(\mathbf{x}_i, \mathbf{x}_0, \omega)$ to this point.

[Figure 3 about here.]

Figure 3a again shows that standard Marchenko estimates are unable to accurately reconstruct the wavefield components attributed to the vertical interfaces. However, comparing Figure 3b and 3c shows that including the true Green's function in equation 7 enables accurate estimation of all wavefield components. These features are confirmed by the trace comparison in Figure 3d. In Figure 3 we have limited the display to source depths of 600 m and below: as already discussed the equations implemented are only valid when the sources are below the receiver positions. Furthermore, for virtual sources at shallow depths the amplitudes are constructed less accurately due to limited apertures; this is because the virtual source locations are closer in terms of depth to the virtual receiver location.

Marchenko Wavefield Estimation

The source-receiver redatuming methods we have so far introduced are of particular interest to geophysicists because they are capable of estimating a full wavefield from any arbitrarily chosen virtual source location inside the subsurface (as virtual receivers can be placed

anywhere in the subsurface). Our suggested methodology incorporates VSP data into this workflow, however we can then no longer place a virtual source arbitrarily in the subsurface. Instead the virtual source must be located at one of the VSP receivers. Nevertheless, virtual receivers can be placed arbitrarily as long as they are placed above the depth level of the virtual source. We have therefore implemented equation 7 for one virtual source location, $\mathbf{x}_j = (1500 \text{ m}, 1296 \text{ m})$, and a grid of virtual receiver locations ($\mathbf{x}_i$), transformed from the frequency to the time domain and the resulting wavefield is shown in Figure 4.

[Figure 4 about here.]

Figure 4 shows the wavefield at six time steps of $\Delta t = 0.1s$. The area of interest is the vertical interface at $x = 1000$ m. Because we have included the VSP data (the true surface-to-subsurface Green's function) in the source-receiver Marchenko method we are able to construct interactions between this feature and the propagating wavefield (blue arrows show the reflection from the vertical interface). Although not shown, the wavefield constructed using standard Marchenko fields is identical except that it does not include these features as they are not included in the input Green's function as shown in Figure 2.

SUBSURFACE IMAGING

So far we have demonstrated a Marchenko method that uses VSP data to estimate Green's functions with improved accuracy over those constructed using existing source-receiver Marchenko methods. In this section we investigate how we can use these estimates to obtain improved images of the subsurface.

VSP Driven Imaging

The aim of seismic imaging is to map subsurface spatial heterogeneities – locations at which seismic waves diffract or reflect. Effectively we are trying to isolate the scattering component of a wavefield and calculate where these components originate. This mapping operation can be defined as (Vasconcelos et al., 2010; Fleury and Vasconcelos, 2012):

$$I_n(\mathbf{x}_k) = G_s(\mathbf{x}_k, \mathbf{x}_k, t = 0) = \int_{-\infty}^{\infty} G_s(\mathbf{x}_k, \mathbf{x}_k, \omega) d\omega, \tag{12}$$

where $G_s(\mathbf{x}_k, \mathbf{x}_k, t)$ is the scattering components of the Green's function with a single co-located source and receiver. The total Green's functions can be related to the scattered Green's function through: $G = G_0 + G_s$, where G_0 is the non-scattered component of the Green's function, calculated here by tracing rays between source and receiver locations. Only if the source/receiver is on a reflector will there be a signal measured at zero time, and hence to construct an image G_s is evaluated at $t = 0$ s. The subscript n is an indexing term to account for the different images produced by equation 12 in the following sections of this article.

In practice, we do not have an accurate measure of G_s, nor do we have a source and receiver at every subsurface location (image point) of interest: to solve equation 12 we need to estimate these. Various imaging conditions are employed in wave-equation based migration techniques to attempt to solve this problem (Jones, 2014). However, in the previous section we have presented a method that accurately estimates wavefields propagating through the subsurface – Green's functions to all points. In equation 12 we therefore choose an imaging condition that exploits this additional information.

Our Marchenko method estimates full Green's functions G. In order to estimate the scattering Green's function we apply a mute to the Green's function such that:

$$G_s(\mathbf{x}_i, \mathbf{x}_j, t) \approx \Psi G(\mathbf{x}_i, \mathbf{x}_j, t), \tag{13}$$

where ΨG is the muted version of the Green's function from equation 9, and the mute removes components that arrive before or at the same time as the direct arrival (plus a small time lag to account for the dominant period of the source term). We can estimate the travel time required to calculate this mute using the reference velocity model, which is already a standard prerequisite for implementing the Marchenko method. Note that this is an approximation as at locations on or near scattering points the mute will also remove components of the scattered Green's function; we return to this below. If the initial velocity model is inaccurate the first arrivals could be manually or automatically picked. However, in this case alternative methods for estimating Green's functions using Marchenko methods when the subsurface velocity model is unknown would need to be applied (e.g. van der Neut and Wapenaar, 2016).

In Figure 4, we showed that Green's functions can be estimated between virtual sources in the well and a variety of virtual receiver locations. Waveforms constructed at each such location contain information about reflections in the subsurface, all of which we would like to use to construct the image. We do this using standard time migration methods applied to all subsurface receiver locations: first we use the reference velocity model to calculate background Green's functions G_0 between the imaging point ($\mathbf{x}_k$) and the source/receiver locations ($\mathbf{x}_j/\mathbf{x}_i$). These can be used to 'redatum' the Green's function by:

$$G_s(\mathbf{x}_k, \mathbf{x}_k, \omega) \approx \int_{\mathbb{D}_i} G_0(\mathbf{x}_k, \mathbf{x}_i, \omega)^* \left[\int_{\partial \mathbb{D}_j} G_s(\mathbf{x}_i, \mathbf{x}_j, \omega) G_0(\mathbf{x}_j, \mathbf{x}_k, \omega)^* d\mathbf{x}_j \right] d^2\mathbf{x}_i, \qquad (14)$$

where $\mathbb{D}_i$ is a volume of virtual receivers at the locations used to construct Figure 4. Equation 14 can then be used to create an image of the subsurface I_1 using equation 12. This imaging condition overcomes the limitations of estimating G_s by applying a mute from equation 13 since almost all of the wavefield components of interest (the scattered components) will be outside of the muted zone (which is calculated using an estimate of the non-scattered components). This methodology is not without its limitations and the amplitudes produced will not be accurate. Equation 14 will not produce images completely free of multiple contamination, however, by including Marchenko Green's functions we are able to redautm the seismic data below the most significant multiple generators and increase the amount of data available to create an image, thus reducing multiple contamination in the result.

We can apply the workflow described above for multiple source locations (the VSP receivers in the well), multiple receiver locations at which we have calculated the wavefield in Figure 4, and an array of image points selected at 8 m intervals in the area defined in Figure 5a. The result of this operation is given in Figure 5b.

[Figure 5 about here.]

The image shown in Figure 5b accurately identifies all of the subsurface interfaces with few artifacts. The VSP data and the complementary surface seismic data are both included in this imaging algorithm; therefore, due to poor illumination points at far offsets from the VSP are imaged less accurately. There is evidence of this in Figure 5b where the horizontal

interface at $z = 450$ between $x = 800$ m $- 1000$ m begins to loose continuity.

Combined Imaging

Given that the image produced in the previous section is limited by the illumination of the VSP it is also of interest to combine this data with surface seismic data which does not suffer from the same illumination issues, but which in theory cannot image the vertical structure of interest. To do so we first implement standard Marchenko imaging using just the surface seismic data from Figure 1. This uses the same imaging condition given in equation 12 and approximates the scattering Green's function as: $G_s(\mathbf{x}_k, \mathbf{x}_0, t) \approx G^-(\mathbf{x}_k, \mathbf{x}_0, t)$, where G^- is calculated using equation 1. This again is an approximation but is sufficient given that G^- will contain the singly reflected components required to create an image. We then apply

$$G_s(\mathbf{x}_k, \mathbf{x}_k, \omega) \approx \int_{\partial \mathbb{D}_0} G^-(\mathbf{x}_k, \mathbf{x}_0, \omega) G_0(\mathbf{x}_0, \mathbf{x}_k, \omega)^* d\mathbf{x}_0. \tag{15}$$

The result of equation 15 can be substituted into equation 12 to create an image I_2. The resulting image is shown in Figure 5c.

Figure 5c shows a clean imaging result with all of the horizontal interfaces illuminated and accurately identified, but as expected, the vertical interface at $x = 1000$ m is not identified. It is clear that there are advantages and disadvantages to each of the images given in Figures 5b and 5c. We therefore propose that these images can be combined to give one imaging result.

A combined imaging condition was proposed by da Costa Filho and Curtis (2016) which is designed to maintain only features that are common to both images. Since in this case we wish to maintain the vertical interface which only appears in one of the images we need to

adopt a slightly different approach. First we apply a one-dimensional phase matching filter to the image I_2 in Figure 5c to ensure the mapped horizontal reflectors match those of I_1 in Figure 5b. We then weight the amplitudes of I_2 to ensure that the two images have similar energy distributions. Finally we sum the result ($I_3 = I_1 + I_2$), which is given in Figure 5d. This result draws on the benefits of both images: continuous horizontal reflectors as well as the vertical interface. It also exhibits a reduction in artifacts due to the increased signal to noise ratio (SNR).

Fault Imaging

The workflow described above provides a method to create images with reduced overburden multiple contamination in areas of structural complexity where there are steeply dipping interfaces such as salt flanks or fault planes. In this section we apply these methods to a more realistic synthetic subsurface model that includes a faulted structure – an adapted version of the Marmousi 2 model (Martin et al., 2006). We have adapted this model by isolating an area of interest and changing the velocity and density values from the original as we are only using acoustic properties. Our motivation was to create a model with a complex target feature (a fault in this case) and encourage multiply scattered waves with high values for acoustic impedance. These are the two problems to which the method we have formulated above should offer a solution. Figure 6a shows the subsurface velocity structure and Figure 6b show the density structure. Figure 6c shows a smoothed version of the subsurface velocity which we use as a reference model for the Marchenko method. Sources were placed on the surface ($z = 0$ m) at 8 m intervals and receivers were placed at each source point as well as at downhole locations ($x = 1600$ m) again at 8 m intervals.

[Figure 6 about here.]

We first use the surface seismic data to create an image of the subsurface as we did to obtain Figure 5c. The purpose of this is to asses the suitability and advantages of implementing Marchenko imaging in this subsurface model. Therefore for comparison we have also included an image created using ray-based migration where we make the approximation:

$$G_s(\mathbf{x}_k, \mathbf{x}_k, \omega) \approx \int_{\partial \mathbb{D}_0} G_0^-(\mathbf{x}_k, \mathbf{x}_0, \omega) G_0(\mathbf{x}_0, \mathbf{x}_k, \omega)^* d\mathbf{x}_0, \tag{16}$$

where

$$G_0^-(\mathbf{x}_k, \mathbf{x}_0, \omega) = \int_{\partial \mathbb{D}_0} R(\mathbf{x}_0, \mathbf{x}_0', \omega) G_0(\mathbf{x}_0', \mathbf{x}_k, \omega)^* d\mathbf{x}_0'. \tag{17}$$

Equations 16 and 17 are intended to approximate conventional migration methods that assume single scattering. A similar approach is taken in previous publications (see da Costa Filho and Curtis (2016) and Meles et al. (2018) for more details). In Figure 7a and 7b we compare the results from the imaging condition in equation 12 using the two scattering Green's function estimates in equation 15 and 16 respectively. The image result is target-oriented as we have only imaged a small portion of the subsurface model from Figure 6.

[Figure 7 about here.]

The results in Figure 7a and 7b show two images of the fault structure shown in Figure 6. Both show accurate images of the spatial heterogeneity with the best results observed in shallow areas. In the deeper parts the illumination deteriorates, in particular illumination of the fault structure which is poorly imaged in both panels. If we compare the two images

it can be seen that the SNR is worse in Figure 7b. This is highlighted by the difference panel in Figure 7c in which we observe many of the anomalous features of Figure 7b. The number of false reflectors is not significant however, which can be attributed to a limited number of high impedance continuous reflectors. Rather, the high impedance reflectors are shallow and discontinuous (see Figure 6) which instead contributes noise to the image in Figure 7b. Nevertheless this example highlights some advantages of Marchenko imaging over conventional migration.

If we follow the same workflow as defined in the previous section for the model defined in Figure 1, but instead apply it to data from the model in Figure 6 we produce the three images shown in Figure 8. The image is targeted around the fault where the illumination using the surface seismic data in Figure 7 was insufficient to resolve the structural features of interest. It can be seen that VSP Marchenko imaging (Figure 8b) and standard Marchenko imaging (Figure 8c) are sensitive to different features marked by red and blue arrows respectively. Note that the middle blue arrow in Figure 8c is an error which is masking the true event which you can see emerges at around (1200 m, 950 m). The result in Figure 8b compared to 8c shows a clearer image of the fault in shallow areas, where primary reflections from the fault are measured at the surface, and illumination from the VSP deteriorates (due to increasing offset). Therefore, when we combine the images (using the workflow defined above) we obtain an enhanced image (Figure 8d) which better resolves the subsurface features when compared to the alternative methods alone.

[Figure 8 about here.]

DISCUSSION

A condition for the application of the subsurface source-receiver method presented in this article is the requirement for the virtual receiver ($\mathbf{x}_i$) to be above the virtual source ($\mathbf{x}_j$). When both of the input fields are Marchenko estimates, both the focusing and Green's functions can be calculated at every point, so these two terms are interchangeable and Green's functions can be calculated between any two points (Singh and Snieder, 2017). However, in our examples it is the Green's function measured at the well location that contains the additional data in which we are interested. The Green's function is calculated between a surface point $\mathbf{x}_0$ and the virtual source position $\mathbf{x}_j$ at the well (the latter is therefore inflexible). As a result, we impose the condition on the depth co-ordinates $i < j$ and only place virtual receivers above the virtual source position. When we produced the images in this article we integrated over multiple VSP receiver positions $\mathbf{x}_j$, each with a different depth coordinate. However, we also integrated over the virtual receiver positions $\mathbf{x}_i$ and this number changes depending on the virtual source location. This leaves the images prone to bias in their amplitudes as near surface image points have a larger number of contributions. In our results we have applied a depth-dependent weighting factor to account for these effects and this was implemented to produce the image in Figure 5. However, this will not undo the bias which will more accurately image near-surface reflectors rather than those in the deeper areas. If this was to be violated and the virtual receiver was below the VSP receivers the focusing term (f^+) would need to be calculated at the VSP receiver and the Green's function would need to be calculated using Marchenko methods at a depth level below this. However, this would forgo the advantages of using the real VSP measurements, and the results from equation 7 would be comparable to those that could be obtained when both of the input fields were calculated using Marchenko methods.

In Figure 7 we have applied standard Marchenko methods to the Marmousi 2 model. The results show that Marchenko imaging improves on conventional methods. However, this does not mean that Marchenko methods redatum Green's functions as accurately in this more complex model as we have demonstrated is possible in simple synthetic models (Figures 2 and 3). In Figure 9 we compare redatumed common virtual receiver gathers from two image point in the model given in Figure 6 $\mathbf{x}_i = (1300\text{ m}, 400\text{ m})$ and $\mathbf{x}_i = (1000\text{ m}, 1100\text{ m})$: the first is relatively shallow and above the fault, the second is deep and below the fault. If we compare the Marchenko Green's functions with the modelled Green's functions there is a good match between Figure 9a and 9b, however this is not the case if we compare Figure 9c and 9d. This poor match can be attributed to difficulty in estimating accurate focusing functions beneath the fault, as the primary reflection from the fault, which is required to construct accurate focusing functions, is not measured at the surface. So although the results we have presented are promising, more in-depth analysis is required in future studies to ascertain how to improve these estimates.

[Figure 9 about here.]

The focus of this article has been on the inclusion of VSP data in the Marchenko method. However, it may be possible to use alternative signals to replace the Green's function term instead of the VSP data in equation 7 – for example, micro-seismic signals. In this case the Green's functions are unlikely to be as numerous or as well distributed as for a VSP dataset. However, during testing for this article, images of the vertical interfaces could be obtained with relatively few VSP Green's functions. Furthermore, if the aim is not to produce an image but rather to estimate a wavefield, this would be possible with only one single Green's function from a subsurface source (assuming complementary surface receivers and surface

seismic reflection data are available).

We have focused on using the estimated Marchenko wavefield for imaging, but the VSP-Marchenko wavefields contain a significant amount of information to which we do not normally have access. It could be possible to exploit that information to invert for subsurface properties, rather than just to image. We have shown that the virtual-source to virtual-receiver Green's functions are accurate so this could be possible although the implications of using a smoothed reference model as input will need to be investigated.

CONCLUSION

We have presented a way to incorporate VSP data into the Marchenko method and Marchenko imaging. The output of this method is an estimate of the subsurface wavefield from a subsurface virtual source, which potentially contains a large amount of information about the properties of the Earth. In numerical examples we successfully used this wavefield to create images of two synthetic subsurface structures. These images contain reduced contamination due to internal multiples and include vertical features that standard Marchenko imaging and reverse time migration would otherwise struggle to identify.

ACKNOWLEDGEMENTS

The authors would like to thank Petrobras and Shell for their sponsorship of the International Centre for Carbonate Reservoirs (ICCR), and for permission to publish this work from the VSP project. We would also like to thank the fellow members of the ICCR and members of the Edinburgh Interferometry Project (EIP) for their numerous fruitful discussions. Finally, we would like to thank Editor-Designate Jeffrey Shragge, the Assistant Editor, the

Associate Editor Faqi Liu, Giovannni Meles, Matteo Ravasi and three anonymous reviewers for their comments which helped to improve this paper. The data used within this chapter were generated with the Madagascar open-source software package freely available from **www.ahay.org**.

REFERENCES

Bakulin, A., and R. Calvert, 2006, The virtual source method: Theory and case study: Geophysics, **71**, no. 4, SI139–SI150.

Behura, J., K. Wapenaar, and R. Snieder, 2014, Autofocus imaging: Image reconstruction based on inverse scattering theory: Geophysics, **79**, no. 3, A19–A26.

Broggini, F., R. Snieder, and K. Wapenaar, 2012, Focusing the wavefield inside an unknown 1D medium: Beyond seismic interferometry: Geophysics, **77**, no. 5, A25–A28.

Curtis, A., and D. Halliday, 2010, Source-receiver wave field interferometry: Physical Review E, **81**, 046601.

Curtis, A., H. Nicolson, D. Halliday, J. Trampert, and B. Baptie, 2009, Virtual seismometers in the subsurface of the Earth from seismic interferometry: Nature Geoscience, **2**, 700.

da Costa Filho, C. A., and A. Curtis, 2016, Attenuating multiple-related imaging artifacts using combined imaging conditions: Geophysics, **81**, no. 6, S469–S475.

da Costa Filho, C. A., G. A. Meles, and A. Curtis, 2017, Elastic internal multiple analysis and attenuation using Marchenko and interferometric methods: Geophysics, **82**, no. 2, Q1–Q12.

da Costa Filho, C. A., M. Ravasi, and A. Curtis, 2015, Elastic P- and S-wave autofocus imaging with primaries and internal multiples: Geophysics, **80**, no. 5, S187–S202.

da Costa Filho, C. A., M. Ravasi, A. Curtis, and G. A. Meles, 2014, Elastodynamic Green's function retrieval through single-sided Marchenko inverse scattering: Physical Review E, **90**, 063201.

Fleury, C., and I. Vasconcelos, 2012, Imaging condition for nonlinear scattering-based imaging: Estimate of power loss in scattering: Geophysics, **77**, no. 1, S1–S18.

Halliday, D., and A. Curtis, 2010, An interferometric theory of source-receiver scattering

and imaging: Geophysics, **75**, no. 6, SA95–SA103.

Hornby, B. E., and J. Yu, 2007, Interferometric imaging of a salt flank using walkaway VSP data: The Leading Edge, **26**, 760–763.

Jones, I., 2014, Tutorial: migration imaging conditions: First Break, **32**, 45–55.

Liu, Y., B. Arntsen, J. van der Neut, and K. Wapenaar, 2018, Up-and downgoing borehole wavefield retrieval using single component borehole and reflection data: Journal of Applied Geophysics, **155**, 256–264.

Liu, Y., J. van der Neut, B. Arntsen, and K. Wapenaar, 2016, Combination of surface and borehole seismic data for robust target-oriented imaging: Geophysical Journal International, **205**, 758–775.

Lomas, A., and A. Curtis, 2019, An introduction to Marchenko methods for imaging: Geophysics, **84**, no. 2, F35–F45.

Malcolm, A. E., B. Ursin, and M. V. De Hoop, 2009, Seismic imaging and illumination with internal multiples: Geophysical Journal International, **176**, 847–864.

Martin, G. S., R. Wiley, and K. J. Marfurt, 2006, Marmousi2: An elastic upgrade for Marmousi: The Leading Edge, **25**, 156–166.

Meles, G. A., K. Löer, M. Ravasi, A. Curtis, and C. A. da Costa Filho, 2014, Internal multiple prediction and removal using Marchenko autofocusing and seismic interferometry: Geophysics, **80**, no. 1, A7–A11.

Meles, G. A., K. Wapenaar, and A. Curtis, 2016, Reconstructing the primary reflections in seismic data by Marchenko redatuming and convolutional interferometry: Geophysics, **81**, no. 2, Q15–Q26.

Meles, G. A., K. Wapenaar, and J. Thorbecke, 2018, Virtual plane-wave imaging via Marchenko redatuming: Geophysical Journal International, **214**, 508–519.

Ravasi, M., 2017, Rayleigh-Marchenko redatuming for target-oriented, true-amplitude imaging: Geophysics, **82**, no. 6, S439–S452.

Ravasi, M., I. Vasconcelos, A. Kritski, A. Curtis, C. A. d. C. Filho, and G. A. Meles, 2016, Target-oriented Marchenko imaging of a north sea field: Geophysical Supplements to the Monthly Notices of the Royal Astronomical Society, **205**, 99–104.

Singh, S., and A. Curtis, 2019, Imaging vertical interfaces using acoustic time reversal: Geophysics, **84**, no. 3, Q1–Q11.

Singh, S., and R. Snieder, 2017, Source-receiver Marchenko redatuming: Obtaining virtual receivers and virtual sources in the subsurface: Geophysics, **82**, no. 3, Q13–Q21.

Singh, S., R. Snieder, J. Behura, J. van der Neut, K. Wapenaar, and E. Slob, 2015, Marchenko imaging: Imaging with primaries, internal multiples, and free-surface multiples: Geophysics, **80**, no. 5, S165–S174.

Singh, S., R. Snieder, J. van der Neut, J. Thorbecke, E. Slob, and K. Wapenaar, 2016, Accounting for free-surface multiples in Marchenko imaging: Geophysics, **82**, no. 1, R19–R30.

Slob, E., and K. Wapenaar, 2017, Theory for marchenko imaging of marine seismic data with free surface multiple elimination: Presented at the 79th EAGE Conference and Exhibition 2017.

Slob, E., K. Wapenaar, F. Broggini, and R. Snieder, 2014, Seismic reflector imaging using internal multiples with Marchenko-type equations: Geophysics, **79**, no. 2, S63–S76.

Thomsen, H. R., F. Broggini, D.-J. van Manen, M. Ravasi, and A. Kritski, 2017, Robust Marchenko focusing-calibrating surface reflection with VSP data: Presented at the 79th EAGE Conference and Exhibition 2017.

Thorbecke, J., E. Slob, J. Brackenhoff, J. van der Neut, and K. Wapenaar, 2017, Imple-

mentation of the Marchenko method: Geophysics, **82**, no. 6, WB29–WB45.

Urruticoechea, C. R., and C. Wapenaar, 2017, Elastodynamic single-sided homogeneous Greens function representation-theory and examples: Presented at the 79th EAGE Conference and Exhibition 2017.

van der Neut, J., and K. Wapenaar, 2016, Adaptive overburden elimination with the multidimensional Marchenko equation: Geophysics, **81**, no. 5, T265–T284.

Van Der Neut, J., K. Wapenaar, J. Thorbecke, and E. Slob, 2015, Practical challenges in adaptive Marchenko imaging, *in* SEG Technical Program Expanded Abstracts 2015: Society of Exploration Geophysicists, 4505–4509.

Vasconcelos, I., P. Sava, and H. Douma, 2010, Nonlinear extended images via image-domain interferometry: Geophysics, **75**, no. 6, SA105–SA115.

Wapenaar, C., and J. Grimbergen, 1996, Reciprocity theorems for one-way wavefields: Geophysical Journal International, **127**, 169–177.

Wapenaar, K., J. Brackenhoff, J. Thorbecke, J. van der Neut, E. Slob, and E. Verschuur, 2018, Virtual acoustics in inhomogeneous media with single-sided access: Scientific reports, **8**, 2497.

Wapenaar, K., F. Broggini, E. Slob, and R. Snieder, 2013, Three-dimensional single-sided Marchenko inverse scattering, data-driven focusing, Green's function retrieval, and their mutual relations: Physical Review Letters, **110**, 084301.

Wapenaar, K., and J. Fokkema, 2006, Green's function representations for seismic interferometry: Geophysics, **71**, no. 4, SI33–SI46.

Wapenaar, K., J. Thorbecke, and J. van der Neut, 2016, A single-sided homogeneous Green's function representation for holographic imaging, inverse scattering, time-reversal acoustics and interferometric Green's function retrieval: Geophysical Supplements to the

Monthly Notices of the Royal Astronomical Society, **205**, 531–535.

Wapenaar, K., J. Thorbecke, J. Van Der Neut, F. Broggini, E. Slob, and R. Snieder, 2014, Marchenko imaging: Geophysics, **79**, no. 3, WA39–WA57.

Wapenaar, K., J. Thorbecke, J. van der Neut, E. Slob, and R. Snieder, 2017, Virtual sources and their responses, part ii: data-driven single-sided focusing: Geophysical Prospecting, **65**, 1430–1451.

Xu, S., and S. Jin, 2006, Wave equation migration of turning waves, *in* SEG Technical Program Expanded Abstracts 2006: Society of Exploration Geophysicists, 2328–2332.

Zuberi, M., and T. Alkhalifah, 2014, Generalized internal multiple imaging: Geophysics, **79**, no. 5, S207–S216.

LIST OF FIGURES

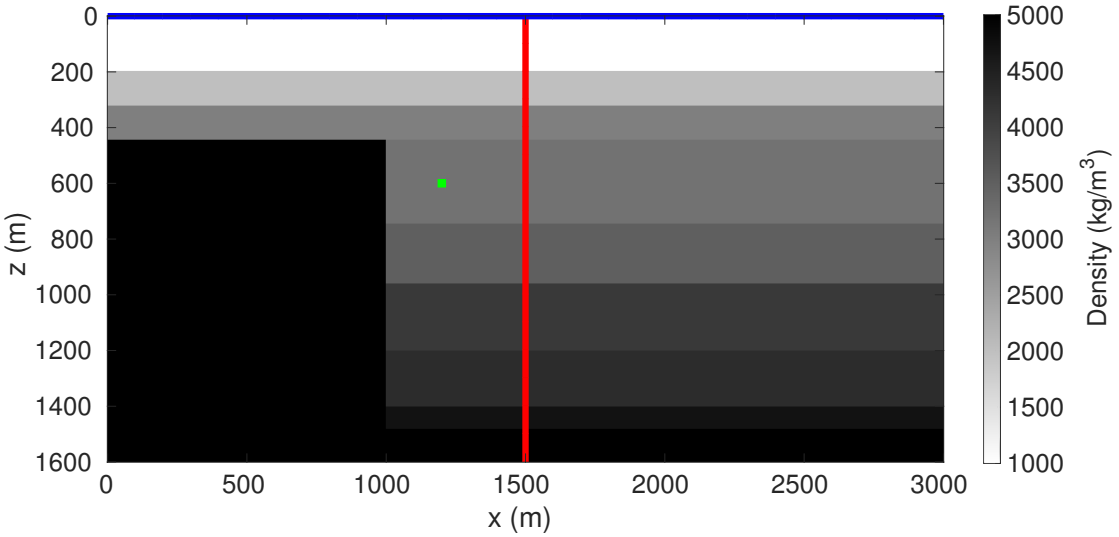

Figure 1: A two-dimensional synthetic variable density, constant velocity ($2500m/s$) subsurface model. Seismic data was simulated on the surface of this model ($z = 0$ m) from co-located sources and receivers along the blue line. A complementary VSP data set was also simulated between sources along the blue line and downhole receivers along the red line. In all cases the source and receiver spacing was 16 m. The green dot at (1200 m, 600 m) is the virtual-source receiver used in Figure 3.

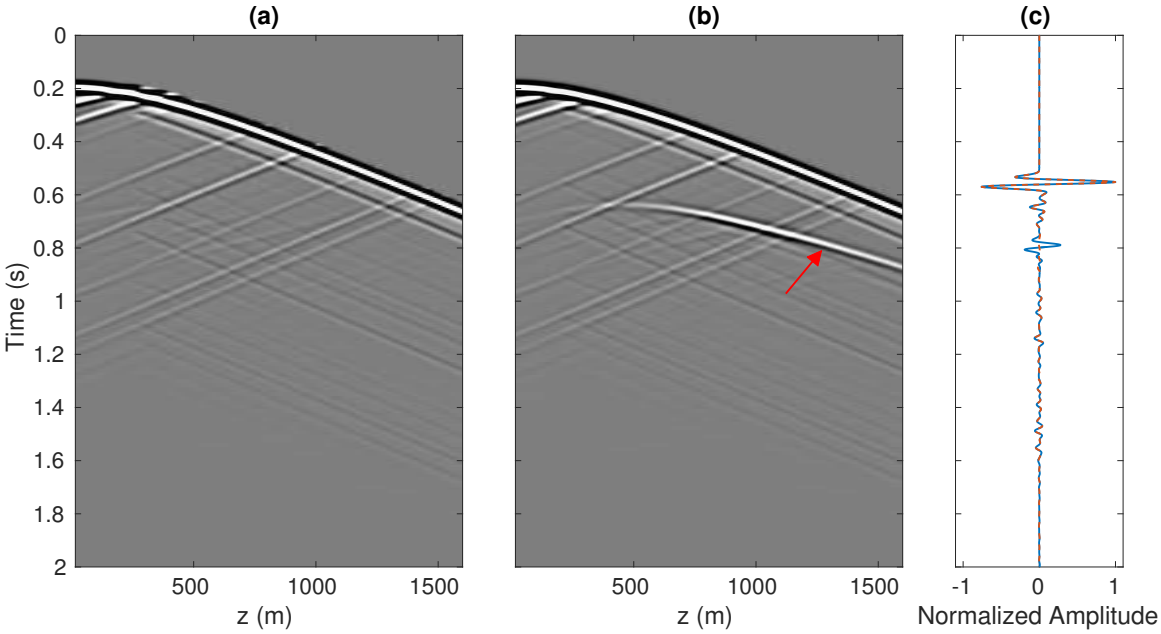

Figure 2: A comparison of Marchenko estimated Green's functions between a source at $x = 2004$ m on the surface and VSP receivers in the well $x = 1500$ m (Figure 1). Panel (a) shows the calculated recordings using Marchenko estimates (virtual receivers) and panel (b) shows the true solution as measured by the VSP. The red arrow indicates an event reflected from the vertical interfaces that is missing from the Marchenko estimate in panel (a). Panel (c) compares a single trace ($z = 1296$ m) for the Marchenko estimated Green's function (orange) and the VSP Green's function (blue): for display purposes this plot has a time dependent gain applied.

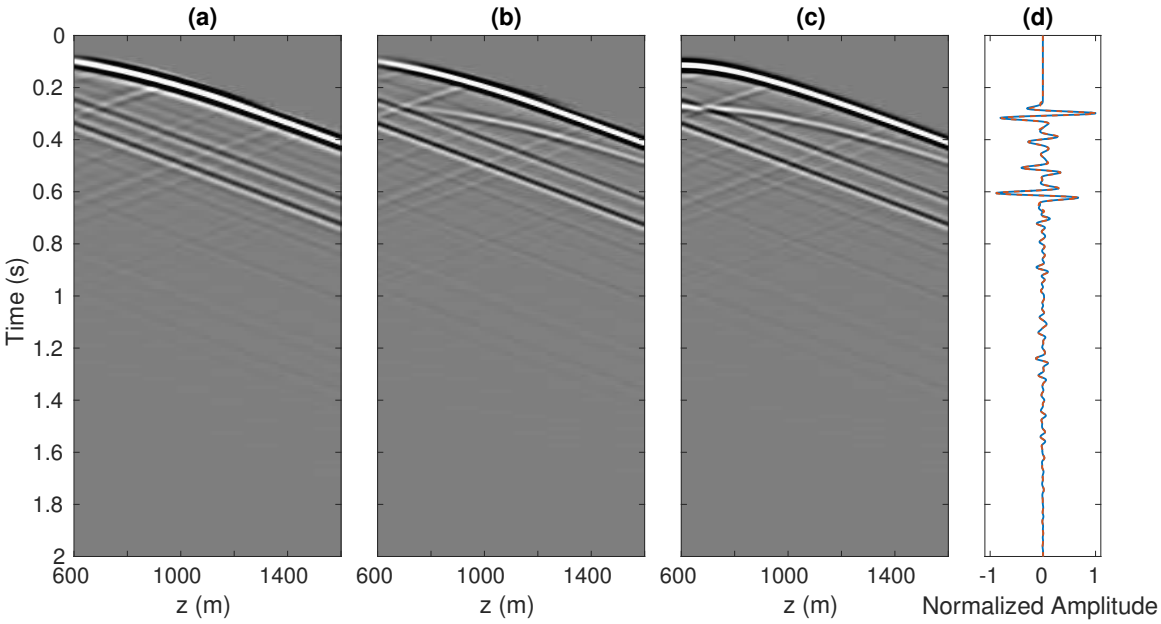

Figure 3: A comparison of Marchenko estimated Green's functions between a virtual receiver at (1200 m, 600 m) and VSP receivers (now virtual sources) in the well $x = 1500$ m (Figure 1). Panel (a) shows the calculated recordings using Marchenko estimates (virtual receivers and virtual sources), panel (b) shows the result using the virtual receiver and VSP receivers, and for comparison panel (c) shows the modelled result between a source at the virtual receiver location and the VSP receivers. Panel (d) compares a single trace ($z = 1296$ m) for the Marchenko estimated Green's function from panel (b) (orange) and the true Green's function using the VSP data from panel (c) (blue): for display purposes this plot has a time dependent gain applied.

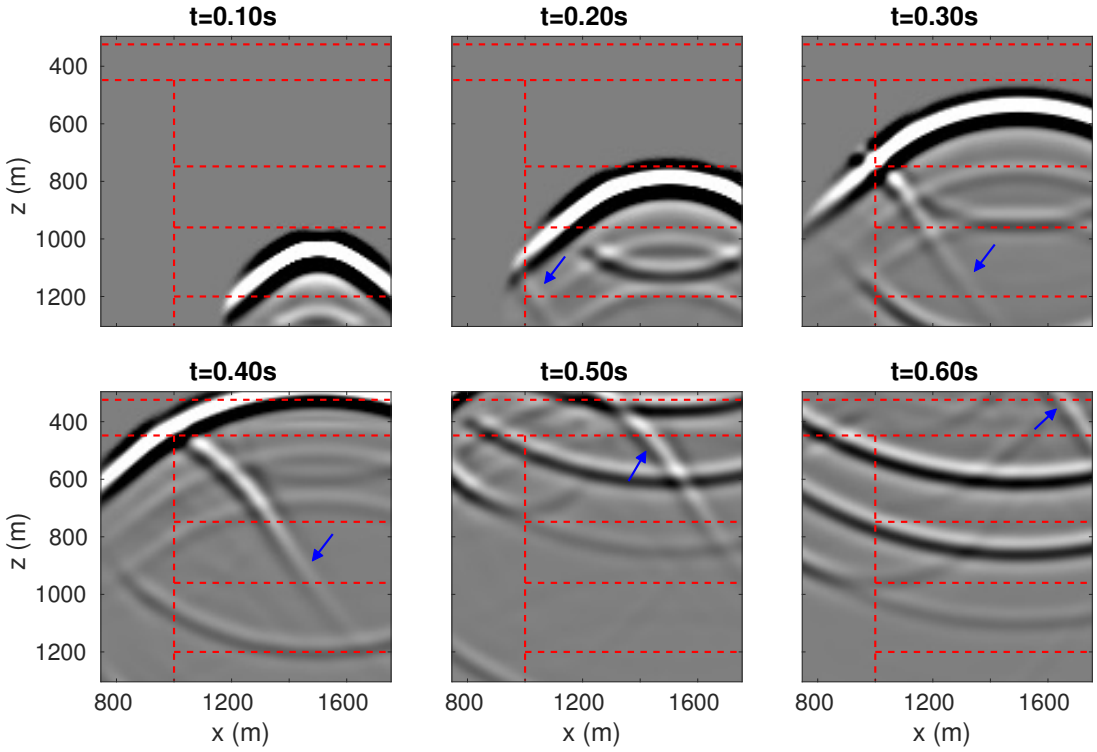

Figure 4: An estimated wavefield from a source at (1296 m, 1500 m) constructed using the virtual source-receiver Marchenko method including VSP data. The panels show the wavefield at time intervals of 0.1 s after the source origin time. The red dashed lines indicate the boundaries of true subsurface density variations and the blue arrows identify the primary reflections from the vertical interface.

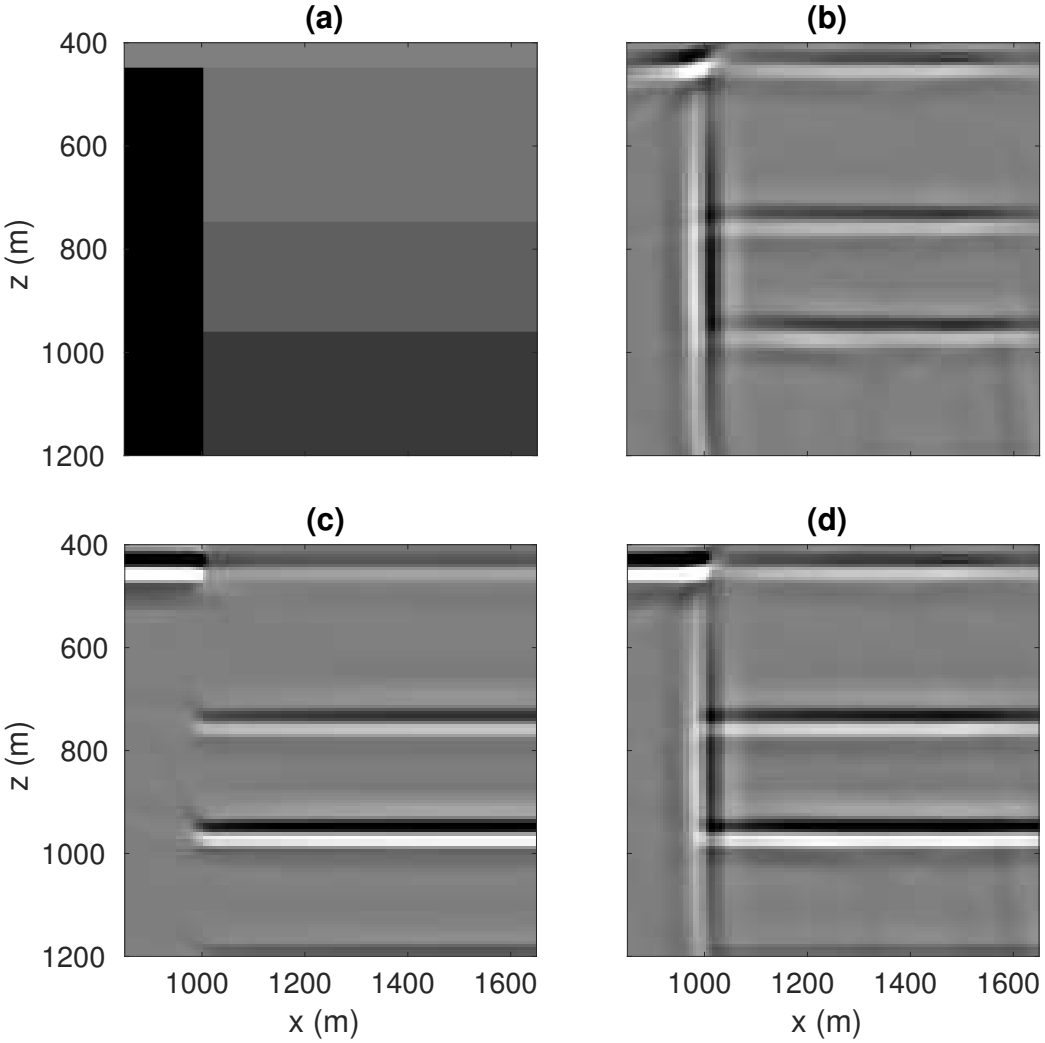

Figure 5: A comparison of images created using the data simulated through the model in Figure 1. Panel (a) shows the imaged area of the subsurface density model. Panel (b) shows imaging results using the VSP data and the imaging condition defined in equations 14 and 12. Panel (c) shows the image produced using standard Marchenko imaging methods (see equation 15). Panel (d) is the weighted sum of panels (b) and (c).

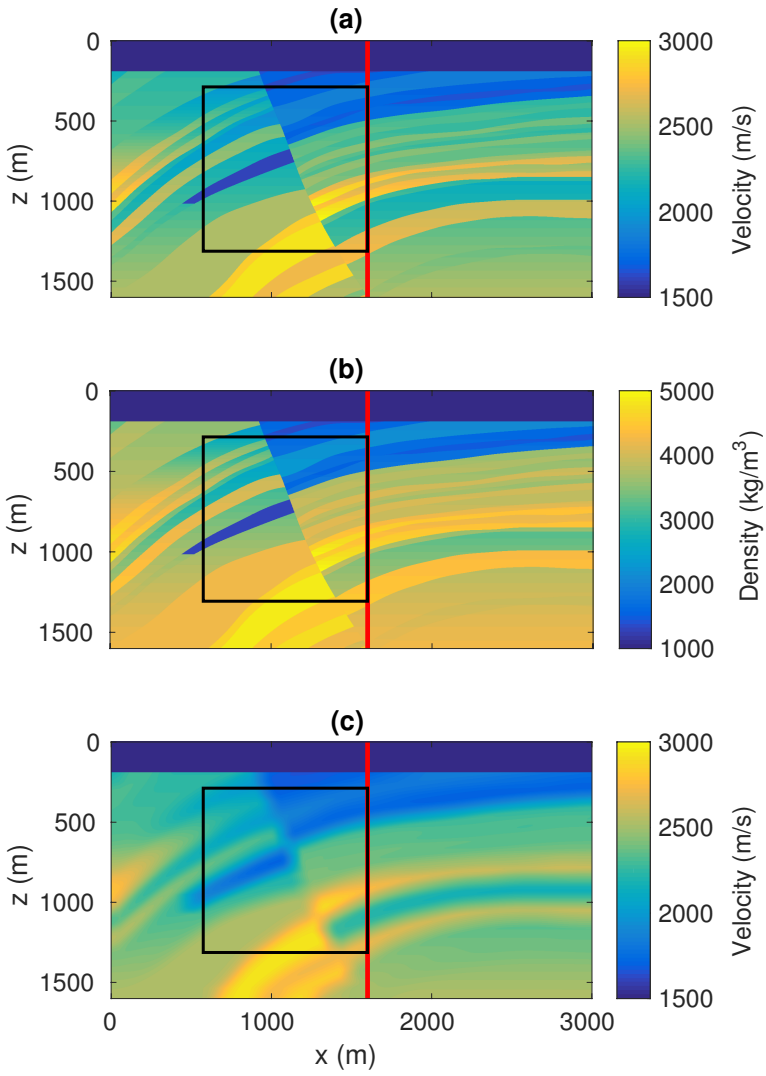

Figure 6: Acoustic properties of a synthetic subsurface model. Panel (a) shows the velocity structure, panel (b) shows the density structure and panel (c) shows a smoothed estimate of the velocity structure. This model is an adapted version of the original Marmousi 2 model. We created synthetic surface seismic data from co-located sources and receivers at 8 m intervals on the surface. Furthermore we created VSP data between the same surface sources and downhole receivers at $x = 1600$ m, spaced at 8 m intervals, indicated by the red line. The black square highlights the area imaged in Figure 7

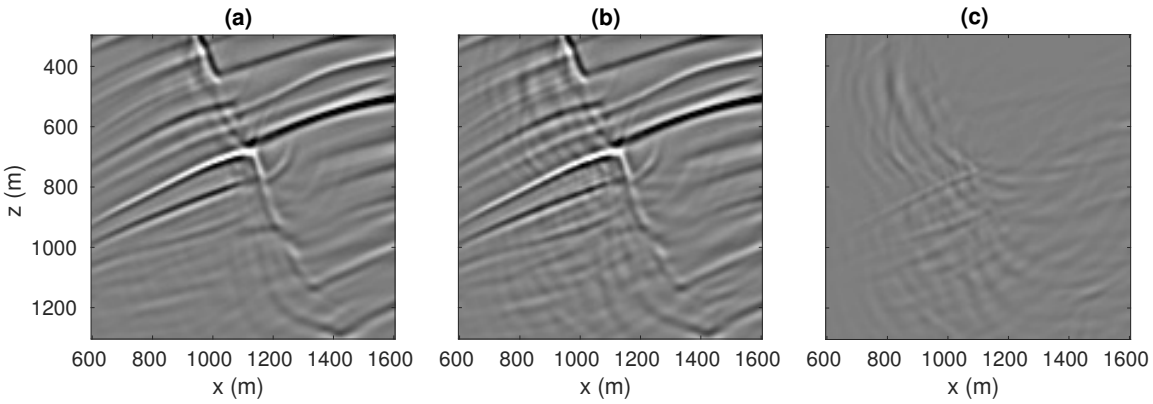

Figure 7: A comparison of images formed using (a) Marchenko Imaging and (b) conventional imaging methods. Both images have been formed using the same imaging condition (equation 12) but different approximations in estimating the scattering Green's function (equation 15 for (a) and equation 17 for (b)). Panel (c) shows the difference between the images, calculated by subtracting panel (a) from panel (b).

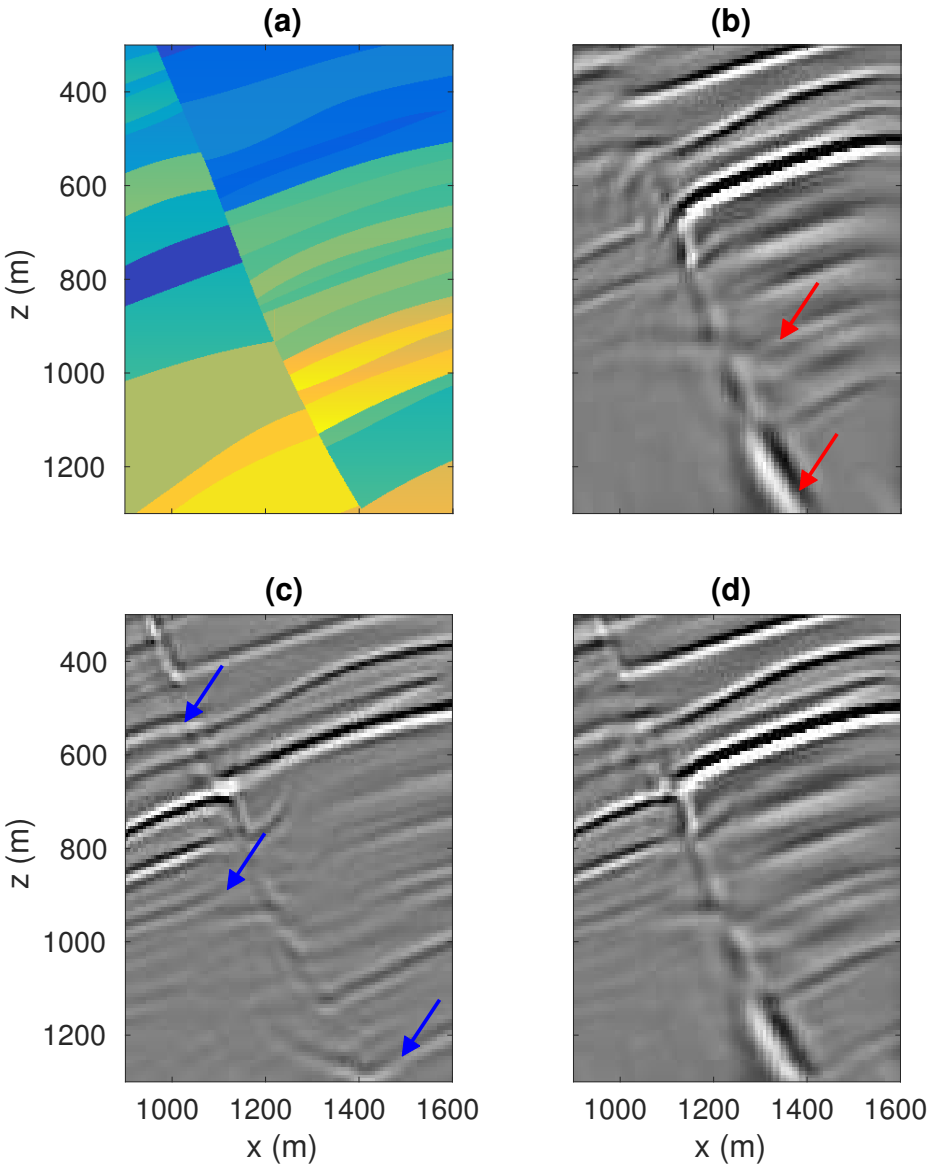

Figure 8: A comparison of images created using: (b) VSP Marchenko imaging, (c) standard Marchenko imaging and (d) combined VSP Marchenko imaging. The results presented in panels (b) and (c) are sensitive to different features so for comparison we have highlighted features unique to the result in panel (b) with red arrows and features unique to panel (c) with blue arrows. The true model from Figure 6 is given for comparison in panel (a).

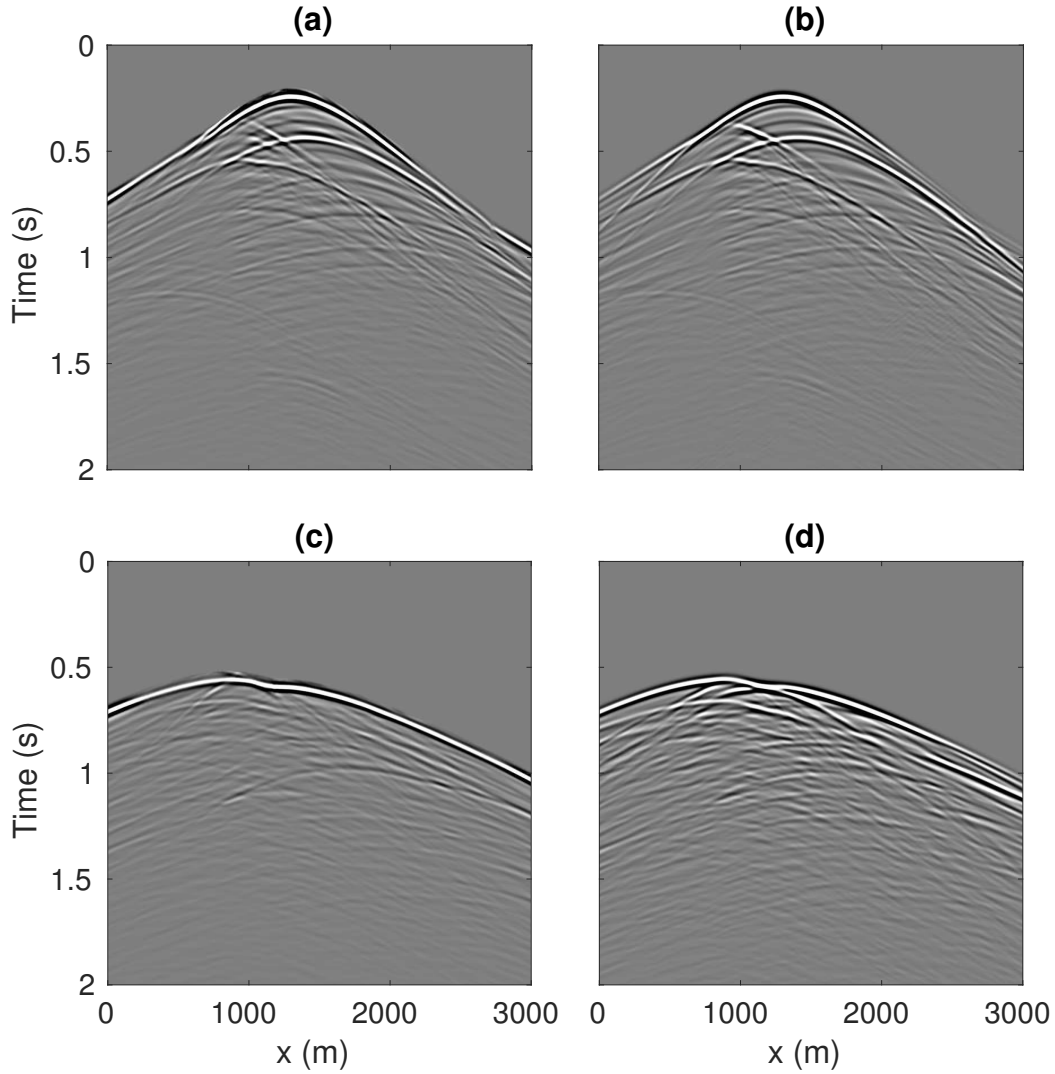

Figure 9: A comparison of Marchenko Green's functions (a and c) and modelled Green's functions (b and d). Panels (a) and (b) are calculated between the surface source array and a virtual receiver position at $\mathbf{x}_i = (1300 \text{ m}, 400 \text{ m})$ in Figure 6. Panels (c) and (d) were calculated between the surface source array and point $\mathbf{x}_i = (1000 \text{ m}, 1100 \text{ m})$.

LIST OF TABLES

	State A	State B
on $\partial\mathbb{D}_0$	$p_A^+ = f_1^+(\mathbf{x}_0, \mathbf{x}_i, \omega)$	$\partial_z p_B^+ = 0$
	$p_A^- = f_1^-(\mathbf{x}_0, \mathbf{x}_i, \omega)$	$\partial_z p_B^- = \partial_z G(\mathbf{x}_0, \mathbf{x}_j, \omega)$
on $\partial\mathbb{D}_i$	$\partial_z p_A^+ = -\frac{1}{2}\iota\omega\rho(\mathbf{x}_i')\delta(\mathbf{x}_i - \mathbf{x}_i')$	$p_B^+ = G^+(\mathbf{x}_i', \mathbf{x}_j, \omega)$
	$\partial_z p_A^- = 0$	$p_B^- = G^-(\mathbf{x}_i', \mathbf{x}_j, \omega)$

Table 1: A comparison of the wavefields $p_{A/B}^{+/-}$, where state A represents the focusing state and state B represents the Green's functions state. These wavefields are evaluated on the boundaries $\partial\mathbb{D}_0$ and $\partial\mathbb{D}_i$.